



## Enhancing summer atmospheric water cycle simulations in the Three-River Headwaters Region via dynamical downscaling

Xuan Liu<sup>a,b,c</sup>, Mingxiang Yang<sup>b,\*\*</sup>, Tinghai Ou<sup>c</sup>, Hui-Wen Lai<sup>c</sup>, Fan Wen<sup>a</sup>, Ningpeng Dong<sup>b</sup>, Hao Wang<sup>b</sup>, Deliang Chen<sup>c,d,\*</sup>

<sup>a</sup> China Three Gorges Corporation, Wuhan, Hubei, China

<sup>b</sup> State Key Laboratory of Simulation and Regulation of Water Cycle in River Basin, China Institute of Water Resources and Hydropower Research, Beijing, China

<sup>c</sup> Department of Earth Sciences, University of Gothenburg, Gothenburg, Sweden

<sup>d</sup> Department of Earth System Sciences, Tsinghua University, Beijing, China

### ARTICLE INFO

#### Keywords:

Dynamic downscaling  
Atmospheric water cycle  
Precipitation recycling  
Three-River Headwaters Region

### ABSTRACT

Characterizing and understanding the evolving water cycle in the Three-River Headwaters (TRH) region of the Tibetan Plateau, where data scarcity poses significant challenges to climate and atmospheric water cycle research, heavily depends on model simulations. However, advanced global climate models and reanalysis datasets frequently overestimate precipitation. To address this, we employ high-resolution (9 km) regional climate simulations (WRF9km) to examine atmospheric water cycle variables in the TRH region, comparing them with in-situ observations and ERA5 reanalysis. Our study demonstrates that WRF9km substantially reduces the overestimation of summer precipitation (by 24.0 %) and evapotranspiration (by 52.7 %) compared to ERA5, thereby improving its alignment with observational data. The reduced biases in precipitation are attributed to diminished moisture influx from the southern boundary and local evapotranspiration, coupled with increased moisture export from the eastern boundary. Summer precipitation recycling (PR) accounts for approximately 20 % of total precipitation in the TRH region. Despite divergent trends in PR between a water accounting model (WAM) and a bulk method, our findings support the reliability of WAM, indicating a slight decrease in summer PR (−0.4 %/10a for ERA5 and −0.6 %/10a for WRF9km). While WRF9km accurately captures the spatial pattern of summer PR, ERA5 appears to overestimate it, likely due to biases in evapotranspiration and moisture inflow. In conclusion, WRF9km provides a more accurate representation of the atmospheric water cycle in the TRH region.

### 1. Introduction

Global warming has induced significant changes in the global water cycle (Olmedo et al., 2022; Yu et al., 2020), affecting key processes such as precipitation, evapotranspiration (ET), and water vapor transport. These changes have important implications for regional climates, potentially accelerating or decelerating the regional water cycle (Gu et al., 2023; Ficklin et al., 2019). Such alterations can lead to increased occurrences of extreme weather events, with profound consequences for critical sectors such as water resources, agriculture, and ecosystems (de Oliveira et al., 2017; Xi et al., 2018). Investigating the dynamics of the atmospheric water cycle at the regional scale is crucial for improving our understanding of complex atmosphere-land interactions and their

effects on precipitation patterns and water resource availability.

Precipitation within a specific region consists of two distinct components:  $P_e$ , representing the internal contribution from local ET processes (Burde and Zangvil, 2001), and  $P_a$ , which refers to external advective water vapor from outside the region (Gimeno et al., 2012; Roy et al., 2018). Precipitation recycling (PR) serves as a valuable metric, measuring the portion of precipitation that originates from local ET processes (Eltahir and Bras, 1996). This metric is essential for assessing the atmospheric water cycle and the interaction between land and atmosphere. In mountainous regions with elevated PR ratios, positive feedback mechanisms reinforce ET contributions to atmospheric moisture, leading to increased precipitation, higher soil moisture levels, and greater ET.

\* Corresponding author at: Department of Earth Sciences, University of Gothenburg, Gothenburg, Sweden.

\*\* Corresponding author.

E-mail addresses: [yangmx@iwhr.com](mailto:yangmx@iwhr.com) (M. Yang), [deliang@gu.se](mailto:deliang@gu.se) (D. Chen).

The Three-River Headwaters (TRH) region, located in the north-eastern Tibetan Plateau (TP), where the Lancang-Mekong, Yangtze, and Yellow Rivers originate, has undergone a significant shift from dry to wet summers over the past four decades (Liu et al., 2023; Shi et al., 2016; Sun et al., 2020). Situated between the mid-latitude westerlies and the monsoons, this region experiences strong moisture feedback, with its precipitation resulting from complex interactions among the westerlies, the Indian monsoon, and PR (Sun and Wang, 2018; Yao et al., 2022). Zhao and Zhou (2021) estimated a summer PR ratio of approximately 23 % for the broader TP, encompassing an area three times larger than that of the TRH region, while Wang (2023) calculated an annual PR ratio of around 20 % specific to the TRH region. Previous studies suggest that the contribution of summer PR to overall precipitation in the TP does not exceed 40 % (Gao et al., 2020), implying that external water vapor transport primarily determines summer precipitation. Indeed, Liu et al. (2023) demonstrated a link between increased TRH summer precipitation and enhanced southerly and easterly water vapor transport from 1979 to 2020. However, a knowledge gap remains in quantifying the changes in the summer atmospheric water cycle, including precipitation, ET, and PR, within the TRH region.

Studying water vapor transport and the contribution of PR to increased precipitation poses challenges, primarily due to data scarcity in the TRH region, where research on the atmospheric water cycle is hindered by the consistent overestimation of precipitation by global climate models and reanalysis datasets. These limitations obstruct a comprehensive understanding of historical and future developments in the atmospheric water cycle in this critical region. To address this gap, a new approach is required, one that relies on high-resolution simulations, as suggested by (Gao et al., 2023; Wei et al., 2023).

In this study, we leverage a high-resolution simulation (9 km) using the Weather Research and Forecasting (WRF) model, spanning the past four decades for the entire TP, hereafter referred to as WRF9km. This model has outperformed satellite-based products in terms of summer precipitation frequencies and diurnal cycles within the TP (Ou et al., 2020). Additionally, it has accurately reproduced the climatological summer precipitation patterns in the northwestern TP with a reduced wet bias (Ou et al., 2023) and has shown significant promise for hydrological applications in the monsoon-dominated southern TP (e.g., Sun et al., 2021). These evaluations demonstrate that WRF9km's precipitation skills align well with the observations in the TP.

This study aims to elucidate the water cycle dynamics associated with variations in TRH summer precipitation over the past decades. Our key objectives are: 1) to evaluate the performance of WRF9km and global reanalysis (ERA5) in representing key elements of the summer water cycle over the TRH region; 2) to quantify changes in the water vapor budget and land-atmosphere interactions using two distinct PR calculation methods; and 3) to assess the added value of high-resolution WRF simulations compared with coarser-resolution global reanalysis in

depicting the atmospheric water balance over the TRH region. Our study not only provides a new perspective on long-term changes in the water cycle over the TRH region but also offers a scientific foundation for developing more reliable climate models and adjusting regional water resource management strategies.

## 2. Data and methods

### 2.1. Observational and reanalysis data

Following Liu et al. (2023), the TRH region was divided into three distinct subregions based on longitude, reflecting the gradual decrease in elevation from west to east. These subregions are the western TRH (WTRH, located west of 94° E), the eastern TRH (ETRH, situated east of 98° E), and the central TRH (CTRH, lying between the WTRH and ETRH), as shown in Fig. 1.

The global climate and weather data from the fifth-generation ECMWF reanalysis (ERA5) integrate modeled data with observations from around the world using physical principles, resulting in a globally complete dataset (Hersbach et al., 2023). For our analysis, we employed the ERA5 reanalysis dataset, which includes pressure-level horizontal wind, specific humidity, surface pressure, precipitation, and ET. This data is available at a monthly resolution and features a grid spacing of 0.25°.

To evaluate the ability of ERA5 (Hersbach et al., 2023) and WRF9km to capture observed seasonal cycles and trends in precipitation and ET within the TRH region, we used gridded monthly observations for precipitation from CN05.1 (Wu and Gao, 2013) and ET from Global Land Evapotranspiration Amsterdam Model (GLEAM) (Martens et al., 2017). GLEAM v3.5 is a suite of algorithms designed to estimate terrestrial ET using satellite data (Martens et al., 2017). Despite some inherent uncertainties, the GLEAM product was considered being able to provide reliable estimates of global evaporation (Miralles et al., 2011). The dataset covers the 42-year period from 1980 to 2021 and has a global resolution of 0.1° × 0.1°. CN05.1 is derived from daily records collected by 2472 rain gauges across China, covering the 58-year period from 1961 to 2018, with a resolution of 0.25° × 0.25° (Wu and Gao, 2013).

The evaluation period extends from 1980 to 2018, while the analysis period spans from 1980 to 2019. For evaluation and comparison purposes, all datasets, including ERA5, WRF9km, and CN05.1, were remapped to a common grid system with a 0.1° × 0.1° resolution using bilinear interpolation.

### 2.2. WRF9km simulations

To provide a high-resolution, long-term simulation, we employed the WRF model in a non-hydrostatic configuration to dynamically down-scale ERA5 reanalysis data. Initial and boundary conditions for the WRF

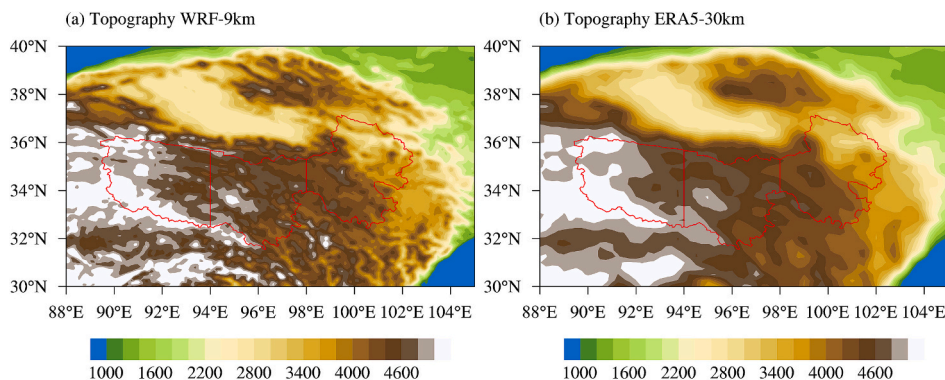


**Fig. 1.** Topography (units: m) of the Three-River Headwaters region (TRH) based on (a) ERA5 and (b) WRF9km. The red line shows the boundary of the TRH. (For interpretation of the references to colour in this figure legend, the reader is referred to the web version of this article.)

model were supplied by the ERA5 dataset. The model domain was centered at coordinates 29.0°N, 95.0°E, consisting of 730 grid points from east to west, 550 grid points from north to south, and included 60 vertical levels extending up to the model's upper boundary at 10 hPa. To improve the representation of seasonal mean precipitation, cumulus parameterization was disabled, enabling the model to better capture summer mean precipitation, as demonstrated by [Ou et al. \(2020\)](#). For more comprehensive details regarding the specific model configuration and parameterization schemes used in this study, please refer to the detailed descriptions in [Ou et al. \(2023\)](#) (Table 1).

This WRF model simulation (WRF9km) provides atmospheric variables, including precipitation, ET, wind, specific humidity, and more, for the TP from 1980 to 2019 at a spatial resolution of 9 km and hourly intervals. This dataset has previously been employed to improve our understanding of various processes, including the diurnal cycles of summer precipitation ([Ou et al., 2020](#)), addressing the wet bias in ERA5 ([Ou et al., 2023](#)), examining the role of Mesoscale Convective Systems ([Kukulies et al., 2021](#)).

### 2.3. CCHZ-DISO

Considering the advancements in big data, the assessment of data quality and model performance has emerged as a critical area of scientific investigation. However, many existing metrics focus on specific aspects of evaluation and lack a comprehensive approach. To address this, we employed a new comprehensive assessment system developed by ([Hu et al., 2022](#)), known as the Chen, Chen, Hu, and Zhou (CCHZ) - Distance Between Indices of Simulation and Observation (DISO), to evaluate the performance of the WRF9km and ERA5 reanalysis data against observational data. The CCHZ-DISO system is based on Euclidean Distance principles, with flexible selection of statistical metrics. Due to its adaptability and simplicity, the CCHZ-DISO system can be applied to any scientific field.

In this study, we used three metrics: spatial correlation coefficient (CC), absolute error (AE), and root-mean-square error (RMSE), to calculate the DISO values.

$$\text{DISO} = \sqrt{(\text{CC} - 1)^2 + (\text{norAE} - 0)^2 + (\text{norRMSE} - 0)^2} \quad (1)$$

where norAE and norRMSE represent the normalized AE and RMSE, calculated by dividing the difference between the maximum and minimum values. A lower DISO index indicates better model performance.

### 2.4. PR models

To investigate the spatiotemporal variation of PR, we used two models: a bulk model ([Brubaker et al., 1993](#)) and the water accounting model (WAM) ([van der Ent et al., 2010](#)). The model developed by Brubaker extends the PR concept introduced by [Budyko \(1974\)](#) to a two-dimensional space. The Brubaker method relies on three key assumptions: 1) local ET and advective water vapor are well-mixed; 2) advective water vapor decreases (while ET increases) linearly from the upstream to the downstream area; and 3) precipitation and ET are uniformly distributed within the study area. In this method, the PR rate

**Table 1**  
WRF9km parameterization schemes.

Names	Parameterization schemes
Long-wave radiation	RRTMG ( <a href="#">Iacono et al., 2008</a> )
Short-wave radiation	New Goddard ( <a href="#">Chou and Suarez, 1999</a> )
Cumulus parameterization	Turned off ( <a href="#">Ou et al., 2020</a> )
Microphysics parameterization	WRF Double Moment 6-class ( <a href="#">Lim and Hong, 2010</a> )
Planetary Boundary Layer	Yonsei University (YSU) ( <a href="#">Hong et al., 2006</a> )
Land surface process	Unified Noah Land Surface layer ( <a href="#">Chen and Dudhia, 2001</a> )

is defined as the ratio of precipitation generated by local ET to the total precipitation. From this definition, it follows that:

$$P = P_a + P_e \quad (2)$$

$$\rho = \frac{P_e}{P} \quad (3)$$

where  $\rho$  is the PR ratio,  $P_a$  is the contribution originating from external advective water vapor (units: mm/d), and  $P_e$  represents the internal contribution originating from local ET processes (units: mm/d). In Brubaker method,  $P_a$ ,  $P_e$ , and  $ET$  are considered constants. Therefore, the evaporative and advective water vapor increase linearly. The outflow of the water vapor fluxes ( $F_{out}$ ), the water vapor transport from advection ( $Q_a$ ), and the water vapor transport from local ET ( $Q_e$ ) can be expressed as:

$$F_{out} = (F_{in} - P_a A) + (ET - P_e) A \quad (4)$$

$$Q_a = \frac{F_{in} + (F_{in} - P_a A)}{2} = F_{in} - \frac{P_a A}{2} \quad (5)$$

$$Q_e = \frac{0 + (ET - P_e) A}{2} = \frac{(ET - P_e) A}{2} \quad (6)$$

where  $F_{in}$  is the inflow of the water vapor fluxes (units: mm/d),  $A$  is the area of the study region (units: m<sup>2</sup>). Based on the well-mixed atmosphere assumption, the ratio of  $P_a$  and  $P_e$  is equal to the ratio of  $Q_a$  and  $Q_e$ .

$$\frac{P_a}{P_e} = \frac{Q_a}{Q_e} = \frac{F_{in} - \frac{P_a A}{2}}{\frac{(ET - P_e) A}{2}} \quad (7)$$

The regional recycling ratio is expressed as follows:

$$\rho = 1 - \frac{P_a}{P} = \frac{ET \bullet A}{ET \bullet A + 2F_{in}} \quad (8)$$

However, the Brubaker model uses area-averaged values of precipitation and ET, meaning that the PR ratio ( $\rho$ ) can only be obtained as an area-averaged value. To overcome this limitation, the WAM model proposed by [Van der Ent et al. \(2010\)](#) can capture the spatial variations of PR using a grid-cell approach. The WAM model is based on the principle of mass conservation, which can also be applied to specific regions:

$$\frac{\partial S_{aloc}}{\partial t} + \frac{\partial S_{aloc} u}{\partial x} + \frac{\partial S_{aloc} v}{\partial y} = E_{loc} - P_{loc} \quad (9)$$

where  $S_{aloc}$  is the atmospheric moisture storage which is originate from local region (here equals to ET),  $E_{loc}$  and  $P_{loc}$  is the ET and precipitation from local region. In this approach, we assume that moisture in the atmosphere is well-mixed, which implies that

$$\frac{S_{aloc}}{S_a} = \frac{\frac{\partial S_{aloc} u}{\partial x}}{\frac{\partial S_a u}{\partial x}} = \frac{\frac{\partial S_{aloc} v}{\partial y}}{\frac{\partial S_a v}{\partial y}} = \frac{P_{loc}}{P} \quad (10)$$

where  $P$  is the precipitation,  $S_a$  is the atmospheric moisture storage. Therefore, the regional PR ratio for a certain region was calculated as follows:

$$\rho_{c_{loc}}(t_{begin-end}, x, y) = \frac{\sum_{t=t_{begin}}^{t_{end}} P(t, x, y) \frac{S_{aloc}(t, x, y)}{S_a(t, x, y)}}{\sum_{t=t_{begin}}^{t_{end}} P(t, x, y)} \quad (11)$$

where  $\rho_{c_{loc}}$  is the local PR ratio. The atmospheric moisture storage can be

obtained by:

$$S_a = \frac{A}{g \cdot \rho_w} \int_0^{p_s} q dp \quad (12)$$

where  $A$  is the area of a grid cell.

It's important to recognize that the models used in this study assume a well-mixed atmosphere. This assumption has implications for the estimation of PR ratios, potentially leading to either underestimation or overestimation, depending on the specific precipitation mechanisms involved (Fitzmaurice, 2007). Underestimation of PR ratios is more likely in cases involving convective precipitation, where intense vertical motions and localized updrafts can decouple near-surface and upper-level air masses. In such cases, the well-mixed atmosphere assumption may not accurately capture the complex vertical moisture transport associated with convective systems. Conversely, overestimation of PR ratios is more likely in cases involving upper-level storms, which can exhibit strong horizontal and vertical moisture advection. In these situations, the well-mixed atmosphere assumption may overemphasize moisture recycling, as it doesn't fully account for the stratification and transport of moisture in the upper troposphere.

In addition to assuming a well-mixed atmosphere, the Brubaker model also postulates the parallel flow of moisture across the study region. In high mountain areas, such as the TRH region, the potential for

underestimation of recycling is particularly relevant due to the complex terrain and the influence of orographic lifting, which can significantly affect precipitation processes. These topographic features can lead to localized variations in atmospheric stability and moisture availability, further challenging the validity of the well-mixed atmosphere assumption.

### 3. Results and discussions

#### 3.1. Evaluation of precipitation and ET from WRF9km and ERA5

We conducted an evaluation of the spatiotemporal distribution of precipitation and ET from both ERA5 and WRF9km against observational data. Notably, the analysis of long-term summer precipitation data reveals an increasing trend in the TRH region during the period from 1980 to 2018, as shown in Fig. 2a. All datasets indicate a significant decadal transition from a dry to a wet regime around 2002, supported by statistical significance ( $P < 0.05$ ). This observation aligns with the findings of Liu et al. (2023). The analysis of ET data based on GLEAM for the study region, as presented in Fig. 2b, also reveals a significant linear trend ( $P < 0.05$ ) over the study period.

To further investigate changes in the atmospheric water balance associated with the observed shifts in summer precipitation patterns, we

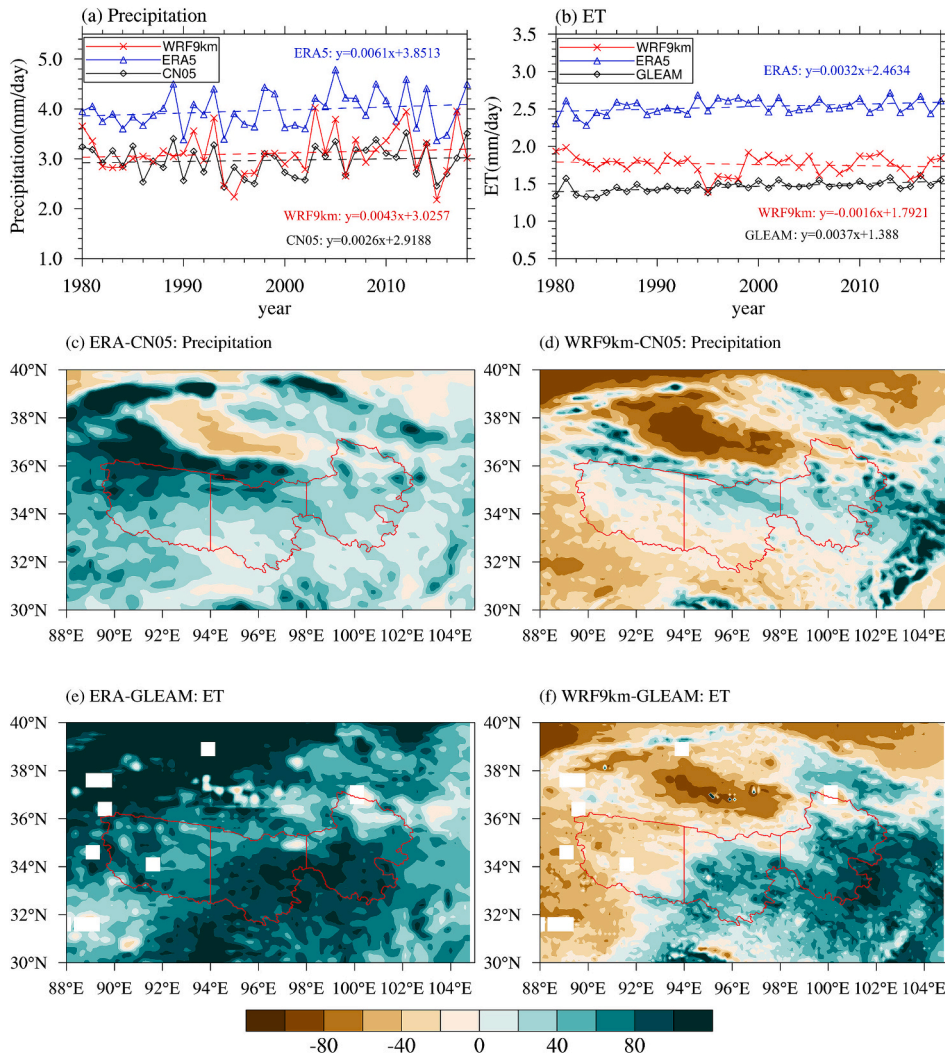


Fig. 2. Time series of standardized (a) TRH summer precipitation and (b) TRH summer ET during 1980–2018 based on observations, ERA5, and WRF9km. Relative differences (units: %) in summer precipitation between (c) ERA5 and CN05.1. Relative differences (units: %) in summer ET between (e) ERA5 and GLEAM. (d) and (f) as in (c) and (e) but for WRF9km.

defined two distinct periods: the “dry period” spanning 1980–2002 and the “wet period” from 2003 to 2018. These periods allow for a focused examination of the changes in water balance dynamics related to the observed summer precipitation shifts in the TRH region.

The temporal DISO indices of TRH regional mean summer precipitation are 0.6 for WRF9km and 1.4 for ERA5 (Table 2), indicating that WRF9km demonstrates superior performance in capturing temporal variation. As shown in Fig. 2a, both ERA5 and WRF9km effectively capture the trend and interannual variability of summer precipitation. However, the magnitude of summer precipitation in WRF9km more closely matches CN05.1, with values of 3.1 mm/day and 3.0 mm/day, respectively, while ERA5 significantly overestimates summer precipitation at 4.0 mm/day. Moreover, the summer precipitation trend in WRF9km (0.043 mm/10a) is more consistent with observations (0.026 mm/10a) compared to ERA5 (0.061 mm/10a). This discrepancy suggests that ERA5 tends to overestimate summer precipitation by nearly 1 mm/day over the TRH region, while WRF9km reduces the wet bias by approximately 24 %.

The spatial pattern of precipitation further shows that ERA5 overestimates precipitation across the entire TRH region, particularly in the northwest, where the relative difference can be as high as 60 % (Fig. 2c), possibly due to its lower resolution. In contrast, WRF9km significantly reduces the wet bias observed in ERA5 (Fig. 2d). The spatial DISO indices are 1.4 for ERA5 and 0.7 for WRF9km, indicating that WRF9km performs better in representing the spatial distribution of summer precipitation than ERA5. This suggests that high-resolution regional climate data, as demonstrated by He et al. (2019), can improve precipitation simulation.

The temporal DISO indices for summer ET are 1.1 for WRF9km and 1.4 for ERA5, indicating better performance of WRF9km in capturing temporal variation. However, in terms of the magnitude of summer ET, ERA5 significantly overestimates ET at 2.5 mm/day, while WRF9km provides a better match with GLEAM at 1.8 mm/day. This indicates that ERA5 overestimates summer ET by about 1 mm/day, while WRF9km reduces the wet bias by approximately 52.7 %. In terms of spatial distribution, WRF9km outperforms ERA5 with a DISO index of 0.7 compared to 1.4 for ERA5. ERA5 overestimates ET across the TRH region, with a relative difference exceeding 60 % in most areas.

Regarding the interdecadal shift in summer precipitation and ET (Fig. A1), neither WRF9km nor ERA5 align well with observed differences between wet and dry periods. While WRF9km reduces the wet bias, it does not fully improve the spatial pattern of the precipitation and ET shifts from dry to wet.

In conclusion, the results collectively indicate that WRF9km is more reliable than ERA5 in reproducing summer precipitation and ET patterns in the TRH region, likely due to its better representation of topographical features. Therefore, WRF9km holds promise for further investigations into variations in the atmospheric water cycle over the TRH region.

### 3.2. Water vapor budget for summer precipitation change

ERA5 and WRF9km exhibit similar spatial patterns in water vapor fluxes and moisture flux convergence (MFC), as shown in Fig. A2. Both datasets display prevailing westerly water vapor fluxes in the TRH region, with positive MFC sustained by westerly and southwesterly inflows. However, WRF9km shows weaker southerly water vapor fluxes

**Table 2**

The DISO values for summer precipitation and evapotranspiration (ET) in the TRH region based on ERA5 and WRF9km.

DISO	Temporal		Spatial	
	Precipitation	ET	Precipitation	ET
ERA5	1.4	1.4	1.4	1.4
WRF9km	0.6	1.1	0.7	0.7

than ERA5. Notably, WRF9km reveals stronger convergence along the northern and southern borders of the TRH region compared to ERA5. These differences may be attributed to WRF’s more accurate representation of water fluxes due to its more realistic terrain depiction.

The differences in water vapor transport and MFC between wet and dry periods provide valuable insights into the role of the water vapor budget in driving changes in TRH summer precipitation (Fig. 3a–b). During the wet period, both WRF9km and ERA5 show anomalous easterly and southerly water vapor fluxes, indicating that enhanced southerly and reduced westerly fluxes contribute to the positive MFC anomaly across much of the TRH region. Furthermore, both datasets demonstrate that changes in MFC exhibit a spatial pattern similar to precipitation changes. This suggests that the transition from dry to wet summer precipitation in the TRH region is likely driven by changes in MFC.

We further examine the differences in boundary water fluxes between wet and dry periods (Fig. 3c–f), using 31.5°–37.0°N and 89.5°–102.5°E as the study area. The results reveal that both ERA5 and WRF9km show positive net water fluxes in the TRH region and its subregions. Water fluxes along the eastern and southern boundaries contribute positively to the increased net water fluxes, while those along the western and northern boundaries contribute negatively. The most significant differences in water vapor fluxes are observed along the eastern boundaries. However, ERA5 suggests a decrease in meridional water fluxes during the wet period, whereas WRF9km shows an increase. Notably, WRF9km exhibits higher disparities compared to ERA5 in the TRH region and its subregions, particularly in water fluxes along the southern boundaries, with values ranging from 0.3 to 0.6 mm/day.

The trends in net water fluxes and boundary water fluxes from ERA5 and WRF9km show similar patterns (Fig. 4). A significant increasing trend is observed in the water fluxes along the eastern boundary in the TRH region based on both ERA5 and WRF9km (1.06 mm/d/a, and 1.30 mm/d/a, respectively,  $p < 0.05$ ), and a decreasing trend is identified along the western boundary (−0.55 mm/d/a, and −0.74 mm/d/a, respectively,  $p < 0.05$ ) and northern boundary (−0.28 mm/d/a, and −0.34 mm/d/a, respectively). This results in a rising trend in net water fluxes (0.19 mm/d/a, and 0.37 mm/d/a, respectively). However, the trends in water fluxes along the eastern, western, and northern boundaries from ERA5 are slightly smaller than those from WRF9km. ERA5 estimates higher water fluxes at the southern and western boundaries of the TRH region and its subregions compared to WRF9km, while presenting lower estimates at the northern and eastern boundaries.

In summary, the results suggest that the primary driver of summer precipitation changes is the increased zonal water flux import, i.e., reduced zonal water vapor flux export. ERA5 tends to overestimate water vapor import from the southern boundary and underestimate water vapor import from the northern boundary. In contrast, WRF9km’s reduced wet biases in summer precipitation are partly due to less water vapor imported from the southern boundary and more water vapor exported from the eastern boundary (Fig. 4).

### 3.3. Changes in PR and the atmospheric water cycle

The investigation into PR using both the WAM and Brubaker methods sheds light on the complex dynamics of the atmospheric water cycle. Fig. 5 provides a comprehensive overview of the summer mean atmospheric water cycle over the TRH region during wet and dry periods, based on ERA5 and WRF9km, using both methods. From 1980 to 2019, the summer PR ratio in the TRH region was approximately 19.4–24.9 %, indicating that summer precipitation is predominantly controlled by external water vapor transport. The estimated summer PR ratio over the TP (23 %) by Zhao and Zhou (2021) and the annual mean PR ratio in the TRH region (21 %) by Wang (2023) are relatively consistent with the findings of this study.

Differences are observed across various models and datasets. Comparing the two PR methods, the summer mean PR ratios from ERA5

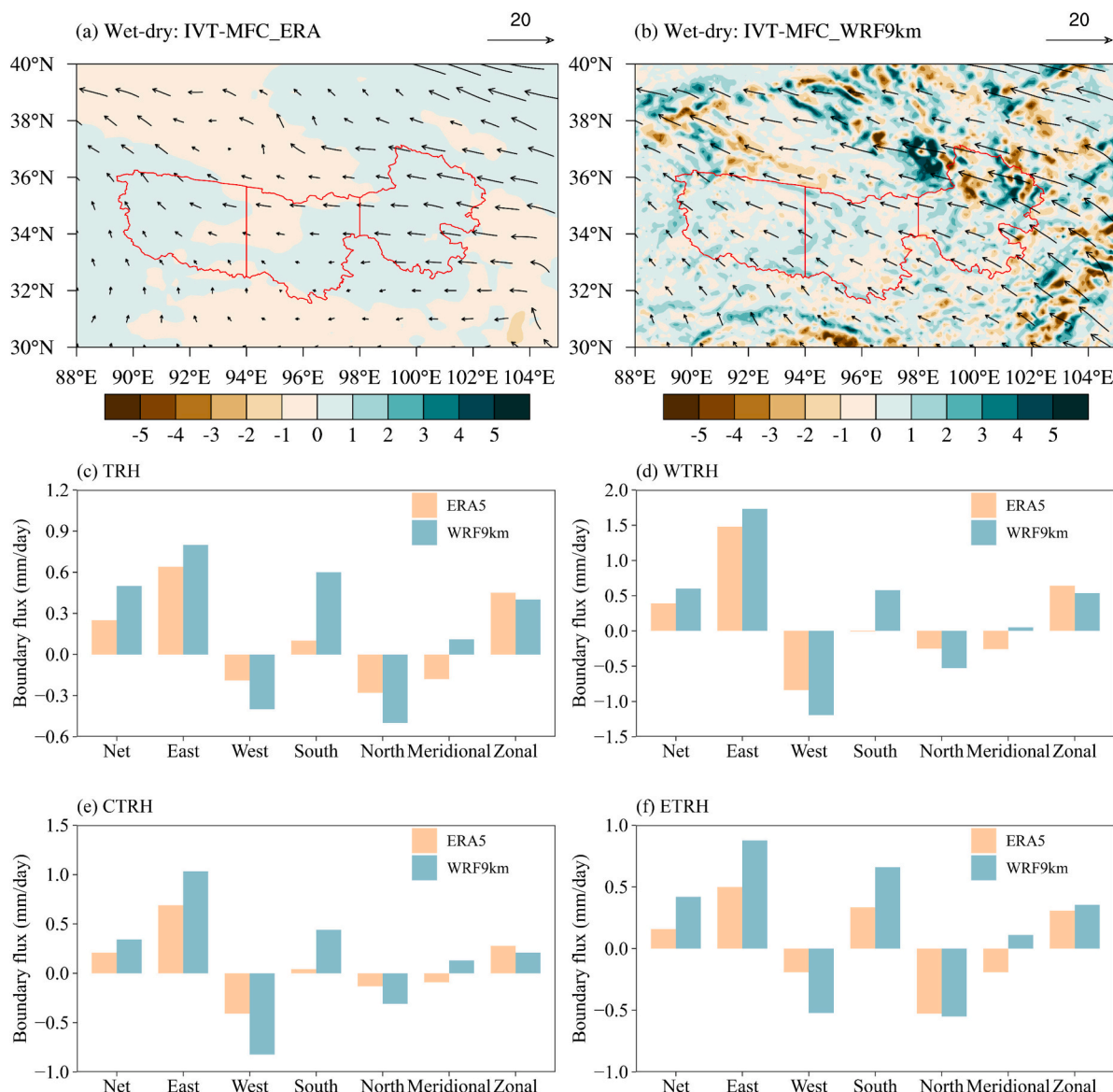


**Fig. 3.** Differences in water vapor flux between wet and dry periods. Differences in water vapor transport (IVT) (vectors, units:  $\text{kg m}^{-1}\text{s}^{-1}$ ) and moisture flux convergence (MFC) (colour, units:  $\text{mm/day}$ ) based on (a) ERA5 and (b) WRF9km. Differences in boundary water flux in the (c) TRH, (d) WTRH, (e) CTRH, and (f) ETRH regions.

and WRF9km using the WAM method were  $25.0\% \pm 2.9\%$  and  $22.0\% \pm 2.3\%$ , respectively, while those using the Brubaker method were  $23.3\% \pm 6.9\%$  and  $18.1\% \pm 4.8\%$ , respectively. The WAM-based PR ratio is higher than the Brubaker-based PR ratio, with the latter exhibiting greater variability. This discrepancy may be attributed to the Brubaker model's emphasis on local ET contributions to precipitation, while the WAM model likely incorporates more factors related to water vapor transport and atmospheric humidity fluctuations.

Furthermore, WRF9km shows close agreement with ERA5, although most values from WRF9km are lower, including the PR ratios. This difference is possibly due to the lower spatial resolution of ERA5, which limits its ability to capture the intricate recycling processes in complex terrain. ERA5 tends to overestimate ET, leading to an overestimation of the contribution of local ET to precipitation. However, WRF9km indicates more external water vapor exits the region, resulting in less external moisture converting into local precipitation compared to ERA5.

During the dry period, summer PR ratios from ERA5 (WRF9km) using the Brubaker method and WAM were  $23.3\%$  and  $25.5\%$  ( $18.0\%$  and  $22.5\%$ ), respectively, while during the wet period, they were  $23.2\%$

and  $24.3\%$  ( $18.3\%$  and  $21.2\%$ ), respectively (Fig. 5). Notably,  $F_{in}$  in the wet period is approximately  $0.06$  to  $0.07$   $\text{mm/d}$  lower than in the dry period, while  $F_{out}$  decreases by about  $0.2$   $\text{mm/d}$ . ET remains largely unchanged. These observations suggest that the observed increase in summer precipitation in the region is primarily attributed to a reduction in  $F_{out}$  and an increase in  $P_a$  within the region.

Additionally, both  $P_a$  ( $0.15$ – $0.20$   $\text{mm/d}$ ) and  $P_e$  ( $0.0$ – $0.05$   $\text{mm/d}$ ) are higher in the wet period than in the dry period. Despite these changes, the PR ratio slightly declines, decreasing by approximately  $-1.3\%$  to  $0.3\%$ . This reduction may be attributed to the increased prominence of external water vapor contributions to total precipitation, overshadowing the role of local ET processes (Wang, 2023). Fig. 6 shows that the contribution of  $P_a$  ( $76.6\%$ – $100.0\%$ ) to the increased precipitation is much larger than that of  $P_e$  ( $0\%$ – $23.4\%$ ). However, even with a marginal decrease in the recycling ratio, the total amount of  $P_e$  actually rises. This increase is facilitated by higher temperatures, which enhance ET rates, augment atmospheric water vapor content, and intensify water vapor exchange rates.

Regarding spatial variations in PR (Fig. 5), ERA5 captures a spatial

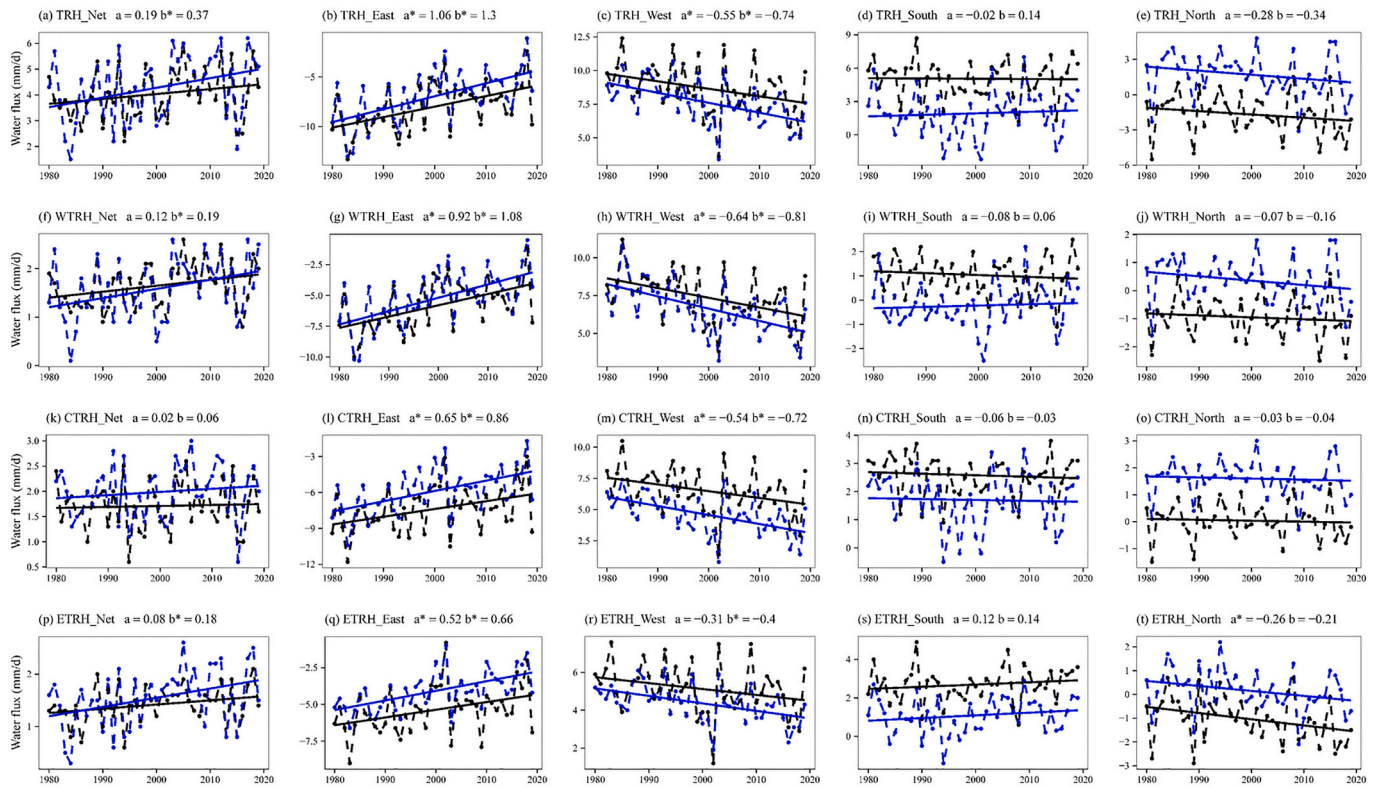


**Fig. 4.** Time series of boundary water fluxes in summer of the TRH region and its subregions (1980–2019). (a–e) for the TRH region, (f–j) for the western TRH (WTRH), (k–o) for the central TRH (CTRH), and (p–t) for the eastern TRH (ETRH). The indices of a and b represent the trends in boundary water fluxes from ERA5 and WRF9km, respectively. The black lines and blue lines represent ERA5 and WRF9km, respectively. The asterisks (\*) indicate that the trend is significant at the 95 % confidence level. (For interpretation of the references to colour in this figure legend, the reader is referred to the web version of this article.)

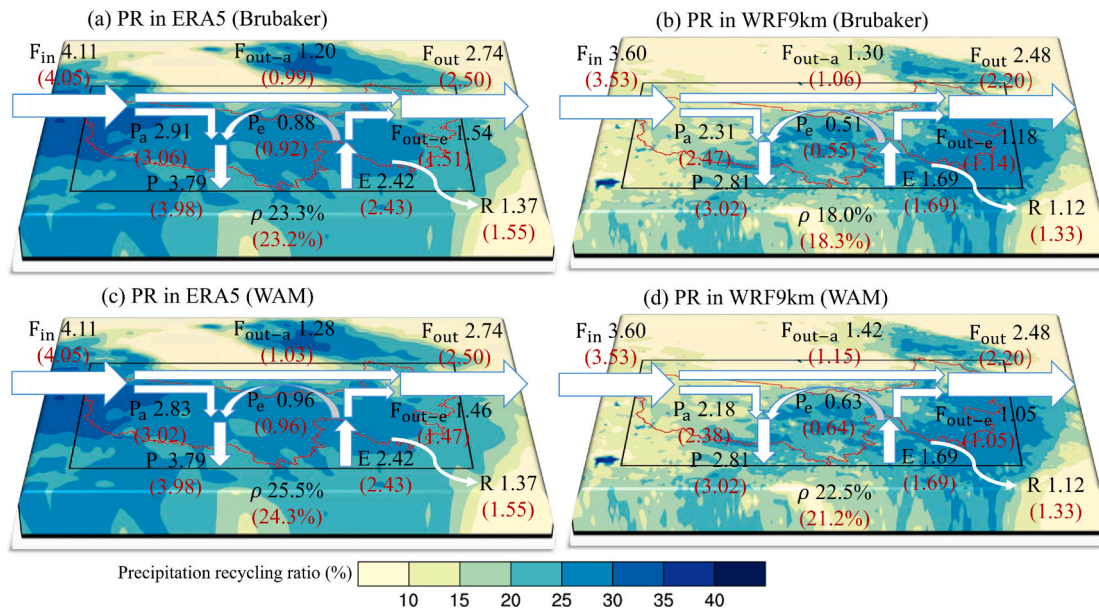


**Fig. 5.** Schematic diagram of the atmospheric water cycle over the TRH region, showing the distribution of summer mean PR ratio (colour, units: %) using the water accounting model (WAM) based on (a, c) ERA5 and (b, d) WRF9km. The black labels denote the dry period and the red labels denote the wet period (units: mm/d). R is runoff,  $F_{out-a}$  is the advected moisture flows out of this region, and  $F_{out-e}$  is the ET flows out of this region. The explanations of the variables (i.e.,  $F_{in}$ ,  $F_{out}$ ,  $P_a$ ,  $P_e$ ,  $P$ ,  $E$ ,  $\rho$ ,  $R$ ) in this figure are provided in Section 2.4. (For interpretation of the references to colour in this figure legend, the reader is referred to the web version of this article.)

gradient in the PR ratio, with the highest values in the northwestern region. In contrast, WRF9km shows a spatial pattern with the highest PR values in the southeastern region, similar to the precipitation

distribution. This spatial distribution of the PR ratio from WRF9km aligns well with a previous study conducted using the ET-tagging method within the WRF model (Shang et al., 2022).

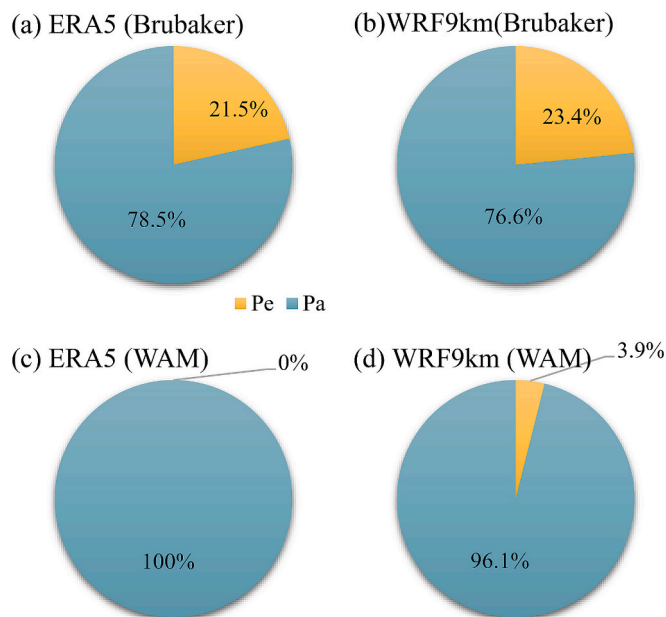


**Fig. 6.** Contribution of precipitation originates from local ET ( $P_e$ ), and from external advective water vapor ( $P_a$ ) to the increased precipitation during wet period. Panels (a) and (c) show results based on ERA5, while panels (b) and (d) depict results from WRF9km. The Brubaker method is applied in panels (a) and (b), and the WAM is utilized in panels (c) and (d).

Regarding temporal variations in PR (Fig. 7a-b), WRF9km aligns well with ERA5 in terms of interannual variation. Both ERA5 and WRF9km, using the WAM method, show a slight decreasing trend in summer PR ratios, with ERA5 at  $-0.4\%/10a$  and WRF9km at  $-0.6\%/10a$ . However, when using the Brubaker method, the summer PR ratios exhibit a slight increasing trend, with ERA5 at  $0.6\%/10a$  and WRF9km at  $0.5\%/10a$ . These trends, although opposite, are not statistically significant. This discrepancy may arise from the different formulas and assumptions underlying each method. The WAM-based PR ratio is negatively related to precipitable water vapor (PWV), which has increased in both ERA5 and WRF9km (Fig. A3), potentially accounting for the decreasing trend in PR ratios using the WAM method. In contrast, the PR ratio estimated by the Brubaker method is positively related to ET and negatively related to moisture inflow. A slight decrease in moisture inflow may explain the increase in PR ratios using the Brubaker method.

Under the Brubaker method, precipitation, ET, and  $P_e$  are considered constant within each grid of the study region, and atmospheric water vapor storage is not accounted for. The WAM method is preferred for PR calculation, as it offers a more comprehensive and accurate representation of the atmospheric water cycle by accounting for variability in precipitation, ET, and  $P_a$ , and including changes in atmospheric water vapor storage. Therefore, further investigation into the differences in PR ratios between wet and dry periods using the WAM method sheds light on the dynamics of the atmospheric water cycle in the study region (Fig. 7c-d). Both ERA5 and WRF9km show a decrease in the PR ratio across most of the TRH region, indicating a reduced contribution of local ET to precipitation during the wet period. Specifically, WRF9km shows a more pronounced decline in the PR ratio in the CTRH, while ERA5 shows a reduction of 1% to 2% across the entire region. The results suggest that the reliance of summer precipitation on local ET diminishes during

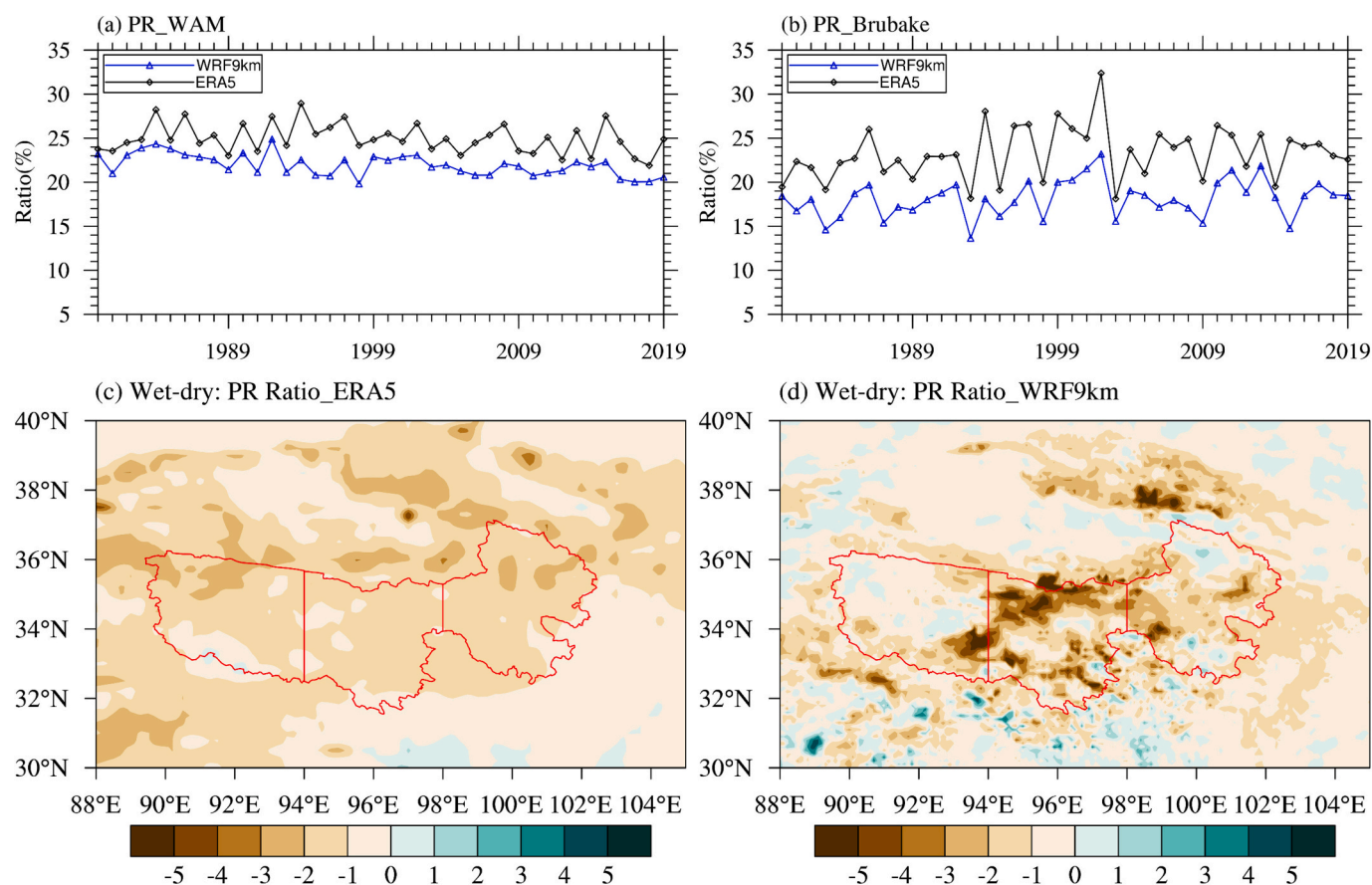


**Fig. 7.** Spatiotemporal variations in TRH summer PR ratio. Time series of summer PR ratio using the (a) WAM and (b) Brubaker method. Differences in the summer PR ratio (units: %) between wet and dry periods based on the (c) ERA5 and (d) WRF9km.

the wet period.

These findings support the idea that the atmospheric water cycle over the TRH region is influenced by complex interactions between moisture sources, transport, and precipitation processes. The decrease in the PR ratio indicates a shift in the dominant moisture source for precipitation, with  $P_a$  playing a more significant role while local ET contributes less to total precipitation. This shift aligns with the observed increase in summer precipitation during the wet period, which is primarily driven by increased  $P_a$ . The WAM-based approach provides a valuable framework for understanding these dynamics and offers insights into the changing patterns of the atmospheric water cycle over the TRH region during different climatic periods.

#### 4. Conclusions

This study conducted a comprehensive analysis of variations in the summer atmospheric water cycle over the TRH region from 1980 to 2019, using data from ERA5 reanalysis and WRF9km downscaled datasets. Both ERA5 and WRF9km generally performed well in simulating key aspects of the atmospheric water balance. WRF9km demonstrated its ability to improve the accuracy of summer precipitation and ET simulations by reducing positive biases, with notable improvements of 24.0 % and 52.7 %, respectively. These improvements can be attributed to several factors, including reduced water vapor import from the southern boundary, increased water vapor export from the eastern boundary, and a decrease in water vapor sourced from local ET processes. However, both ERA5 and WRF9km face challenges in accurately capturing the spatial patterns of summer precipitation and ET changes between wet and dry periods.

Our study suggests that the atmospheric water cycle may not have undergone significant intensification in recent decades, and the TRH summer PR is estimated at approximately 20 %. Additionally, the use of the WAM method over the Brubaker method for PR calculations is preferred in the TRH region, as it offers a more comprehensive and accurate representation of atmospheric water cycle dynamics. Notably, the increased summer precipitation during the wet period is primarily driven by heightened contributions of external advective water vapor to precipitation rather than ET, particularly due to increased zonal water flux import and reduced easterly water flux export.

While ERA5 remains valuable for large-scale, long-term climate change analysis, this study highlights potential limitations in its representation of certain aspects of the regional atmospheric water cycle. Specifically, ERA5 likely overestimates summer PR and displays unrealistic spatial patterns of summer PR in the TRH region. In contrast, high-resolution dynamical downscaling with WRF performs well in capturing the spatial patterns of summer PR and provides a more detailed and likely more realistic representation of changes in water vapor transport contributing to summer precipitation variability, particularly at the boundaries. This underscores the advantages of using dynamical downscaling models for more accurate and detailed simulations of regional atmospheric water cycle dynamics, especially in regions with complex terrain and localized climatic features like the TRH region.

#### CRedit authorship contribution statement

**Xuan Liu:** Writing – original draft, Data curation, Conceptualization. **Mingxiang Yang:** Funding acquisition, Conceptualization. **Tinghai Ou:** Writing – review & editing, Software, Data curation. **Hui-Wen Lai:** Writing – review & editing, Investigation. **Fan Wen:** Visualization, Validation. **Ningpeng Dong:** Methodology, Visualization. **Hao Wang:** Supervision, Funding acquisition. **Deliang Chen:** Writing – review & editing, Supervision, Funding acquisition, Conceptualization.

#### Declaration of competing interest

The authors declare no competing financial interests or personal relationships that could have influenced the work reported in this paper.

#### Data availability

WRF9km datasets are available at <http://biggeo.gvc.gu.se/TPReanalysis/>. ERA5 datasets are available at <https://doi.org/10.24381/cds.6860a573>. The GLEAM datasets are openly available at <https://www.GLEAM.eu>.

#### Acknowledgements

This research was supported by project of State Key Laboratory of Simulation and Regulation of Water Cycle in River Basin (WR110146B0062024), Multi-scale prediction technology and platform for upstream water inflow in plateau lakes: A case study of Siling Co Basin (WR110145B0112024), Science and Technology Project of China Huaneng “Research on Integrated Meteorology and Hydrology Forecasting System in Lancang River Basin” (HNKJ21-HF241), Swedish National Strategic Research Area MERGE and STINT (CH2019-8377 and CH2020-8767), China Power Construction Corporation Technology Project (DJ-HXGG-2021-04) and Key R&D Plan Project in Yunnan Province (202203AA080010).

#### Appendix A. Supplementary data

Supplementary data to this article can be found online at <https://doi.org/10.1016/j.atmosres.2024.107810>.

#### References

- Brubaker, K.L., Entekhabi, D., Eagleson, P.S., 1993. Estimation of continental precipitation recycling. *J. Clim.* 6, 1077–1089. [https://doi.org/10.1175/1520-0442\(1993\)006<1077:EOCPR>2.0.CO;2](https://doi.org/10.1175/1520-0442(1993)006<1077:EOCPR>2.0.CO;2).
- Budyko, M., 1974. *Climate and Life*. New York Academic Press.
- Burde, G.I., Zangvil, A., 2001. The estimation of regional precipitation recycling. Part I: review of recycling models. *J. Clim.* 14, 2497–2508. [https://doi.org/10.1175/1520-0442\(2001\)014<2497:TEORPR>2.0.CO;2](https://doi.org/10.1175/1520-0442(2001)014<2497:TEORPR>2.0.CO;2).
- Chen, F., Dudhia, J., 2001. Coupling an advanced land surface–hydrology model with the Penn State–NCAR MM5 modeling system. Part II: preliminary model validation. *Mon. Weather Rev.* 129 (4), 587–604. [https://doi.org/10.1175/1520-0493\(2001\)129<0569:CAALSH>2.0.CO;2](https://doi.org/10.1175/1520-0493(2001)129<0569:CAALSH>2.0.CO;2).
- Chou, M.D., Suarez, M.J., 1999. A Solar Radiation Parameterization for Atmospheric Studies[R].
- de Oliveira, V.A., de Mello, C.R., Viola, M.R., Srinivasan, R., 2017. Assessment of climate change impacts on streamflow and hydropower potential in the headwater region of the Grande river basin, Southeastern Brazil. *Int. J. Climatol.* 37, 5005–5023. <https://doi.org/10.1002/joc.5138>.
- Eltahir, E.A.B., Bras, R.L., 1996. Precipitation recycling. *Rev. Geophys.* 34, 367–378. <https://doi.org/10.1029/96RG01927>.
- Ficklin, D.L., Abatzoglou, J.T., Novick, K.A., 2019. A new perspective on terrestrial hydrologic intensity that incorporates atmospheric water demand. *Geophys. Res. Lett.* 46, 8114–8124. <https://doi.org/10.1029/2019GL084015>.
- Fitzmaurice, J.A., 2007. *A Critical Analysis of Bulk Precipitation Recycling Models* (Thesis). Massachusetts Institute of Technology.
- Gao, Y., Chen, F., Miguez-Macho, G., Li, X., 2020. Understanding precipitation recycling over the Tibetan Plateau using tracer analysis with WRF. *Clim. Dyn.* 55, 2921–2937. <https://doi.org/10.1007/s00382-020-05426-9>.
- Gao, Z., Yan, X., Dong, S., Luo, N., Song, S., 2023. Object-based evaluation of rainfall forecasts over eastern China by eight cumulus parameterization schemes in the WRF model. *Atmos. Res.* 284, 106618. <https://doi.org/10.1016/j.atmosres.2023.106618>.
- Gimeno, L., Stohl, A., Trigo, R.M., Dominguez, F., Yoshimura, K., Yu, L., Drumond, A., Durán-Quesada, A.M., Nieto, R., 2012. Oceanic and terrestrial sources of continental precipitation. *Rev. Geophys.* 50, RG4003. <https://doi.org/10.1029/2012RG000389>.
- Gu, L., Yin, J., Slater, L.J., Chen, J., Do, H.X., Wang, H.-M., Chen, L., Jiang, Z., Zhao, T., 2023. Intensification of global hydrological droughts under anthropogenic climate warming. *Water Resour. Res.* 59, e2022WR032997. <https://doi.org/10.1029/2022WR032997>.
- He, J., Zhang, F., Chen, X., Bao, X., Chen, D., Kim, H.M., Lai, H.-W., Leung, L.R., Ma, X., Meng, Z., Ou, T., Xiao, Z., Yang, E.-G., Yang, K., 2019. Development and evaluation of an ensemble-based data assimilation system for regional reanalysis over the Tibetan Plateau and surrounding regions. *J. Adv. Model. Earth Syst.* 11, 2503–2522. <https://doi.org/10.1029/2019MS001665>.

- Hersbach, H., Bell, B., Berrisford, P., Biavati, G., Horányi, A., Muñoz Sabater, J., Nicolas, J., Peubey, C., Radu, R., Rozum, I., Schepers, D., Simmons, A., Soci, C., Dee, D., Thépaut, J.-N., 2023. ERA5 monthly averaged data on pressure levels from 1940 to present. In: Copernicus Climate Change Service (C3S) Climate Data Store (CDS). <https://doi.org/10.24381/cds.6860a573>.
- Hong, S.Y., Noh, Y., Dudhia, J., 2006. A new vertical diffusion package with an explicit treatment of entrainment processes. *Mon. Weather Rev.* 134 (9), 2318–2341. <https://doi.org/10.1175/MWR3199.1>.
- Hu, Z., Chen, D., Chen, X., Zhou, Q., Peng, Y., Li, J., Sang, Y., 2022. CCHZ-DISO: a timely new assessment system for data quality or model performance from Da Dao Zhi Jian. *Geophys. Res. Lett.* 49. <https://doi.org/10.1029/2022GL100681>.
- Iacono, M.J., Delamere, J.S., Mlawer, E.J., Shephard, M.W., Clough, S.A., Collins, W.D., 2008. Radiative forcing by long-lived greenhouse gases: calculations with the AER radiative transfer models. *J. Geophys. Res. Atmos.* 113 (D13), 2008JD009944. <https://doi.org/10.1029/2008JD009944>.
- Kukulies, J., Chen, D., Curio, J., 2021. The role of mesoscale convective systems in precipitation in the Tibetan Plateau region. *JGR-Atmos.* 126. <https://doi.org/10.1029/2021JD035279>.
- Lim, K.S., Hong, S.Y., 2010. Development of an effective double-moment cloud microphysics scheme with prognostic Cloud Condensation Nuclei (CCN) for weather and climate models. *Mon. Weather Rev.* 138 (5), 1587–1612. <https://doi.org/10.1175/2009MWR2968.1>.
- Liu, X., Yang, M.-X., Dong, N.-P., Xie, W.-N., Li, H.-G., Guan, Z., Wen, F., Wang, H., Chen, D., 2023. Increased southerly and easterly water vapor transport contributed to the dry-to-wet transition of summer precipitation over the Three-River Headwaters in the Tibetan Plateau. *Adv. Clim. Chang. Res.* 14, 502–510. <https://doi.org/10.1016/j.accre.2023.07.005>.
- Martens, B., Miralles, D.G., Lievens, H., van der Schalie, R., de Jeu, R.A.M., Fernández-Prieto, D., Beck, H.E., Dorigo, W.A., Verhoest, N.E.C., 2017. GLEAM v3: satellite-based land evaporation and root-zone soil moisture. *Geosci. Model Dev.* 10, 1903–1925. <https://doi.org/10.5194/gmd-10-1903-2017>.
- Miralles, D.G., De Jeu, R.A.M., Gash, J.H., Holmes, T.R.H., Dolman, A.J., 2011. An application of GLEAM to estimating global evaporation. *Hydrol. Earth Syst. Sci. Discuss.* 8 (1), 1–27. <https://doi.org/10.5194/hessd-8-1-2011>.
- Olmedo, E., Turiel, A., González-Gambau, V., González-Haro, C., García-Espriu, A., Gabarró, C., Portabella, M., Corbella, I., Martín-Neira, M., Arias, M., Catany, R., Sabia, R., Oliva, R., Scipal, K., 2022. Increasing stratification as observed by satellite sea surface salinity measurements. *Sci. Rep.* 12, 6279. <https://doi.org/10.1038/s41598-022-10265-1>.
- Ou, T., Chen, D., Chen, X., Lin, C., Yang, K., Lai, H.-W., Zhang, F., 2020. Simulation of summer precipitation diurnal cycles over the Tibetan Plateau at the gray-zone grid spacing for cumulus parameterization. *Clim. Dyn.* 54, 3525–3539. <https://doi.org/10.1007/s00382-020-05181-x>.
- Ou, T., Chen, D., Tang, J., Lin, C., Wang, X., Kukulies, J., Lai, H.-W., 2023. Wet bias of summer precipitation in the northwestern Tibetan Plateau in ERA5 is linked to overestimated lower-level southerly wind over the plateau. *Clim. Dyn.* <https://doi.org/10.1007/s00382-023-06672-3>.
- Roy, T., Martinez, A., Herrera-Estrada, J., Zhang, Y., Dominguez, F., Berg, A., Ek, M., Wood, E., 2018. Role of moisture transport and recycling in characterizing droughts: perspectives from two recent u.s. droughts and the CFSv2 system. *J. Hydrometeorol.* 20. <https://doi.org/10.1175/JHM-D-18-0159.1>.
- Shang, S., Arnault, J., Zhu, G., Chen, H., Wei, J., Zhang, K., Zhang, Z., Laux, P., Kunstmann, H., 2022. Recent increase of spring precipitation over the Three-River Headwaters region—water budget analysis based on global reanalysis (ERA5) and ET-tagging extended regional climate modeling. *J. Clim.* 35, 3599–3617. <https://doi.org/10.1175/JCLI-D-21-0829.1>.
- Shi, H., Li, T., Wei, J., Fu, W., Wang, G., 2016. Spatial and temporal characteristics of precipitation over the Three-River Headwaters region during 1961–2014. *J. Hydrol. Reg. Stud.* 6, 52–65. <https://doi.org/10.1016/j.ejrh.2016.03.001>.
- Sun, B., Wang, H., 2018. Interannual variation of the spring and summer precipitation over the Three River Source Region in China and the associated regimes. *J. Clim.* 31, 7441–7457. <https://doi.org/10.1175/JCLI-D-17-0680.1>.
- Sun, J., Yang, K., Guo, W., Wang, Y., He, J., Lu, H., 2020. Why has the Inner Tibetan Plateau become wetter since the mid-1990s? *J. Clim.* 33, 8507–8522. <https://doi.org/10.1175/JCLI-D-19-0471.1>.
- Sun, H., Su, F., He, Z., Ou, T., Chen, D., Li, Z., Li, Y., 2021. Hydrological evaluation of high-resolution precipitation estimates from the WRF model in the Third Pole river basins. *J. Hydrometeorol.* <https://doi.org/10.1175/JHM-D-20-0272.1>.
- van der Ent, R.J., Savenije, H.H.G., Schaeffli, B., Steele-Dunne, S.C., 2010. Origin and fate of atmospheric moisture over continents: origin and fate of atmospheric moisture. *Water Resour. Res.* 46. <https://doi.org/10.1029/2010WR009127>.
- Wang, Z., 2023. Enhanced atmospheric water cycle processes induced by climate warming over the three rivers source region. *Atmos. Res.* <https://doi.org/10.1016/j.atmosres.2023.107040>.
- Wei, J., Arnault, J., Rummeler, T., Fersch, B., Zhang, Z., Olschewski, P., Laux, P., Dong, N., Yang, Q., Xing, Z., Li, X., Yang, C., Zhang, X., Ma, M., Gao, L., Xu, L., Yu, Z., Kunstmann, H.G., 2023. Acceleration of the hydrological cycle under global warming? An age-weighted regional water tagging approach (preprint). <https://doi.org/10.22541/essoar.168500299.99709434/v1>.
- Wu, J., Gao, X., 2013. A gridded daily observation dataset over China region and comparison with the other datasets. *Chin. J. Geophys.* 56, 1102–1111. <https://doi.org/10.6038/cjg20130406>.
- Xi, Y., Miao, C., Wu, J., Duan, Q., Lei, X., Li, H., 2018. Spatiotemporal changes in extreme temperature and precipitation events in the three-rivers headwater region, China. *J. Geophys. Res. Atmos.* 123, 5827–5844. <https://doi.org/10.1029/2017JD028226>.
- Yao, T., Bolch, T., Chen, D., Gao, J., Immerzeel, W., Piao, S., Su, F., Thompson, L., Wada, Y., Wang, L., Wang, T., Wu, G., Xu, B., Yang, W., Zhang, G., Zhao, P., 2022. The imbalance of the Asian water tower. *Nat. Rev. Earth Environ.* <https://doi.org/10.1038/s43017-022-00299-4>.
- Yu, L., Josey, S.A., Bingham, F.M., Lee, T., 2020. Intensification of the global water cycle and evidence from ocean salinity: a synthesis review. *Ann. N. Y. Acad. Sci.* 1472, 76–94. <https://doi.org/10.1111/nyas.14354>.
- Zhao, Y., Zhou, T., 2021. Interannual variability of precipitation recycle ratio over the Tibetan Plateau. *Geophys. Res. Atmos.* 126. <https://doi.org/10.1029/2020JD033733>.